JOURNAL OF SOLID STATE CHEMISTRY 90, 234–248 (1991)

Observation of Ordering in Silicon and Germanium Mullites

A. KAHN-HARARI,*,† S. ABOLHASSANI, D. MICHEL,
L. MAZEROLLES, R. PORTIER, AND J. G. PEREZ-RAMIREZ‡

Laboratoire de Chimie Appliquée de l'Etat Solide CNRS URA302, C.E.C.M., 15 Rue Georges Urbain, 94407 Vitry, France;
**ENSCP 11 Rue Pierre et Marie Curie, 75005 Paris, France; and*
‡*Instituto de Fisica, UNAM A.P. 20-364, 01000 Mexico City, D.F., Mexico*

Received April 25, 1990

The local order is studied in silicon and germanium mullites $Al_{4+2x}M_{2-2x}O_{10-x}$ (M = Si or Ge) using high resolution transmission electron microscopy. A superstructure is observed for $x = 0.5$ and a structural model is proposed from image simulation. Images reconstructed after selecting the diffuse scattering located in the (010) reciprocal plane reveal short range ordered domains for compositions with a low concentration of oxygen vacancies ($x < 0.40$). © 1991 Academic Press, Inc.

Introduction

Mullite $Al_{4+2x}Si_{2-2x}O_{10-x}$ is the crystalline constituent of porcelains and a key material in the ceramic industry. It is the only compound formed at atmospheric pressure in the Al_2O_3–SiO_2 system (*1–4*). The composition range observed for natural and synthetic mullites extends approximately from 58 to 76 mol% Al_2O_3 ($0.17 < x < 0.59$) (*5, 6*). A mullite phase exists also in the Al_2O_3–GeO_2 system, the composition range of which is different from that of silicon mullites and extends at high temperatures without discontinuity from Al_2GeO_5 ($x = 0$) to $2Al_2O_3$–GeO_2 ($x = 0.40$) (*7, 8*).

Three Al_2SiO_5 polymorphs—andalusite, sillimanite, and kyanite—are known in addition to mullite in the Al_2O_3–SiO_2 system, but they are only stable at high pressures (*9, 10*). The structures of mullite and sillimanite are so closely related that they can be considered as isomorphous although their chemical compositions are different (*11–16*). Both structures are orthorhombic with close a and b lattice constants. They consist of chains of AlO_6 edge-sharing octahedra running parallel to the c axis. These octahedral chains are cross-linked by chains of AlO_4 and SiO_4 tetrahedra. Sillimanite is a stoichiometric Al_2SiO_5 compound with ordering of aluminum and silicon atoms on tetrahedral sites (*17, 18*). Mullite, however, is a nonstoichiometric phase $Al_{4+2x}Si_{2-2x}O_{10-x}$ having oxygen vacancies and a variable Al/Si ratio on tetrahedral sites. The Al and Si tetrahedra are no longer ordered at long range and consequently the c lattice constant of mullite is approximately half that of sillimanite.

The structure of $Al_{4+2x}Si_{2-2x}O_{10-x}$ mullites derives from that of sillimanite $Al_4Si_2O_{10}$ by a higher Al/Si ratio and consequently a removal of oxygen atoms from the network.

† To whom correspondence should be addressed.

0022-4596/91 $3.00

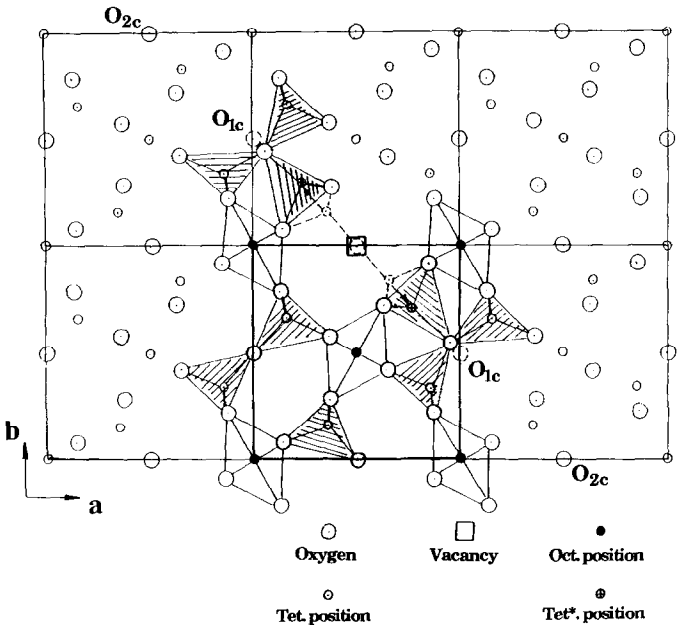

FIG. 1. Projection of the structure of mullite on (001) showing the environment of an oxygen vacancy. Broken lines represent normal positions of atoms before the creation of O_c vacancies. First neighbors of these vacancies are shifted from their normal site, in order to satisfy the fourfold coordination of adjacent cations.

As shown in Fig. 1, oxygen vacancies are located at the common corner of two tetrahedra, positions usually called O_c. In order to maintain a tetrahedral coordination, cations in the vicinity of an oxygen vacancy are shifted to new tetrahedral Tet* sites. Ylä-Jääski and Nissen (*19*) pointed out that the first neighboring O_{1c} sites (Fig. 1) on either side of a vacancy along [110] must be occupied to ensure a fourfold coordination of these Tet* atoms and that the second neighboring O_{2c} sites (Fig. 1) are also occupied, otherwise O_{1c} atoms would be bonded to four cations resulting in unbalanced local charges. These requirements limit the vacancy ratio on O_c sites to one third ($x < 0.67$). Various authors have reported the formation of silica-free mullite either from quenching alumina cryolithe melts (*20*) or from coprecipitation (*21, 22*). In fact, these mullite phases have possibly an impure Al_2O_3 composition, but they are stabilized by small amounts of fluoride or hydroxide ions leading to $Al_6(O, OH, \text{or } F)_{10-x}$ type compositions with $x < \frac{2}{3}$. The formulas $Al_9O_{13}OH$ or $Al_9O_{13}F$ would thus correspond to the limit composition.

Besides the limited number of vacancies, a minimum of local charge imbalance would result if all tetrahedral sites surrounding O_{1c} atoms are occupied only by Al atoms. If this configuration also has to be satisfied, the vacancy ratio will be limited to $\frac{1}{4}$ ($x < 0.5$). It should be noted that x is less than 0.5 for most of the silicon and germanium mullites studied and therefore some cation ordering can occur around vacancies.

The average structure of Si mullite is known from X-ray diffraction studies on single crystals. Atomic positions and site occupancies were refined from the intensities of Bragg reflections (*23–26*). Results for Ge

mullite are very similar to those obtained for Si phases (*27, 28*). In addition to the fundamental reflections corresponding to the space group *Pbam* assigned to mullite, diffuse scattering is observed on X-ray and electron diffraction patterns (*6, 11, 13, 16, 19, 29–35*). These extra features are more or less diffuse, depending on the composition and thermal history of samples. Models for the distribution of oxygen vacancies have been proposed by some authors from the analysis of this diffuse scattering (*32–34*) or from using direct observation by high resolution transmission electron microscopy (HRTEM) (*19, 35, 36*). Recently, J. D. C. McConnell and V. Heine applied a symmetry analysis for incommensurate modulated structures to describe the Al–Si and oxygen vacancy ordering patterns and to explain the stability of mullite (*37*). These previous works have determined the general scheme of ordering in silicon mullites; in particular H. Saalfield (*34*) and J. Ylä-Jääski and H. U. Nissen (*19*) have proposed models of superstructures for highly oxygen-deficient mullites. However, local atomic arrangements are incompletely established for compositions with low amounts of oxygen vacancies. The present paper reports on observation of various states of order in both germanium and silicon phases from HRTEM and analysis of the diffuse scattering using digital image processing.

Experimental

Sample Preparation

Silicon mullite crystals and oriented mullite-glass composites are prepared from directional solidification using a floating zone device associated with a double ellipsoid image furnace as described in a previous paper (*38*). Under our experimental conditions, single phase crystals are only obtained close to the 2 : 1 ratio ($x = 0.40$). For 3 : 2 and Si richer starting compositions, melt samples consist of an Al-rich glass (10–12 mol% Al_2O_3) and mullite crystals with compositions ranging from 62 to 66 mol% Al_2O_3 ($0.30 < x < 0.38$). These results are similar to those reported by Guse and Mateika on Czochralski-grown specimens (*39*). In the case of composite materials, mullite crystals are isolated from glass by a selective attack with hydrofluoric acid. These have a needle-like morphology with growth direction of ⟨001⟩ and lateral faces {110} and typical dimensions about $5 \times 5 \times 200$ μm.

Germanium mullites are not prepared from the melt owing to the high vapor pressure of GeO_2. A wet route is used to obtain better homogeneity. Gels are prepared by coprecipitation with ammonium hydroxide at pH ~10 from a solution of hydrated aluminum nitrate and GeO_2 (quartz form, soluble in hot water). Mullite powders are then obtained by heat-treatment at temperatures between 1100 and 1550°C. For temperatures higher than 1200°C, powders are heated in sealed platinum tubes to prevent germanium dioxide loss.

Chemical Analysis and X-Ray Characterization

Mullite lattice constants are calculated by least square refinement from powder diffraction spectra. Chemical analyses are performed in a transmission electron microscope (JEOL 2000 FX) equipped with an X-ray dispersive energy spectrometer (TRACOR). EDS spectra were calibrated using the stoichiometric compounds Al_2SiO_5 (natural sillimanite) and $Al_2Ge_2O_7$ (*40, 41*) as standards. These analyses show a satisfactory chemical homogeneity in samples and confirm that the measured composition is in agreement with that expected from the values of the unit-cell parameters.

Transmission Electron Microscopy (TEM)

High resolution images are obtained from a JEOL 200 CX 200-kV microscope with a spherical aberration coefficient $C_s = 1$ mm.

Digitized images with a size of 512 × 512 pixels can be recorded with a LHESA video camera and transferred to a VAX 750 computer for subsequent processing using the SEMPER software. Specific programs have been developed to carry out various filtering processes to the Fourier transform of an image before its reconstruction by Fourier inversion.

Through defocus–through thickness simulation of HRTEM images is carried out with a program based on a Bloch wave formalism (*42*). The beam divergence and the chromatic defocus are estimated to be respectively 1 mrad and 7.5 nm.

Results and Discussion

Composition and Unit-Cell Constants

Germanium mullites $Al_{4+2x}Ge_{2-2x}O_{10-x}$ with compositions corresponding to 1 : 1, 3 : 2, and 2 : 1 Al_2O_3/GeO_2 molar ratios (x = 0.0, 0.25, and 0.40 respectively) were specifically studied. For the three compositions, local EDS analyses of crystals in TEM confirm that samples prepared at 1550°C are single phased. Lattice constants are plotted versus composition in Fig. 2a. Within experimental errors, our results are in good agreement with those previously reported by Perez y Jorba (*7*). The composition range of germanium mullite is narrower at 1300°C, as found by the above author. After annealing at 1300°C, samples with a global 1 : 1 composition in fact consist of 3 : 2 mullite (x = 0.25) and a germanium-rich glassy phase.

Silicon mullite crystals are prepared in the composition range $0.30 < x < 0.45$ owing to limitations imposed by their growth from the melt. The variation of unit-cell parameters is linear as shown in Fig. 2b and is in good agreement with previous results of Cameron (*6*).

Electron Diffraction Study of Diffuse Scattering

The diffuse features observed either by X-ray or electron diffraction are mainly located in the (010) plane. This particular plane was searched in both Ge and Si mullites on crushed samples by tilting the TEM specimen holder.

The values of a^* and b^* being very close and the space group *Pbam* imposing similar reflection conditions for h and k ($h = 2n$ for $h0l$ or $k = 2n$ for $0kl$), in the absence of diffuse scattering during the observation, it is not possible to select (010) or (100) planes without ambiguity. Careful measurements of the a^*/c^* or b^*/c^* on films allow the two

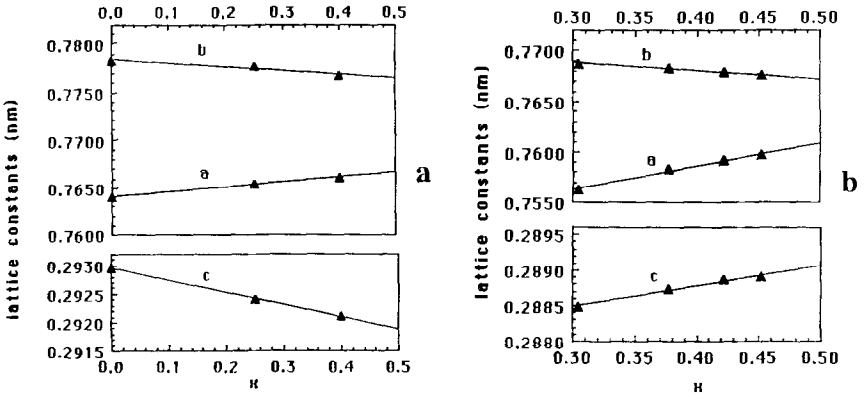

FIG. 2. Variation with composition of unit-cell parameters for (a) germanium mullites $Al_{4+2x}Ge_{2-2x}O_{10-x}$ prepared at 1550°C; (b) silicon mullites $Al_{4+2x}Si_{2-2x}O_{10-x}$ prepared from the melt.

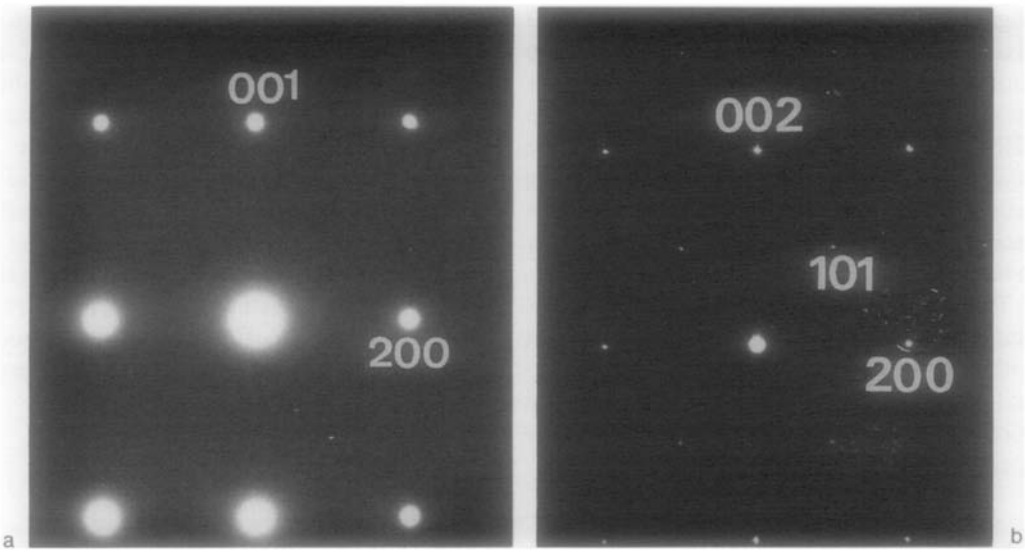

FIG. 3. Electron diffraction patterns of (010) planes: (a) Al_2GeO_5 mullite prepared at 1550°C; (b) Al_2SiO_5 sillimanite. The difference in indexing is due to the value of the c parameter in sillimanite, which is approximately double that of mullite.

to be distinguished afterward. However, the observation of diffuse scattering is a direct indication of the (010) orientation of the specimen.

No diffuse scattering is observed on germanium mullite in the (010) plane when $x = 0$. The corresponding electron diffraction pattern is represented in Fig. 3a. This confirms that Al and Ge atoms are not ordered in Al_2GeO_5 as concluded from vibrational spectra by Perez y Jorba *et al.* (*43*), unlike Al_2SiO_5 sillimanite, where cations alternate in tetrahedral positions along [001]. In sillimanite, because of the doubling of the c spacing and the *Pbnm* space group (*Pnma* in a standard setting after permutation of axes), a diffraction spot 101 is present at the $1,0,\frac{1}{2}$ mullite position, as shown on Fig. 3b. If any ordering, however limited, existed on the cationic sublattice of Al_2GeO_5, the significant difference in the atomic scattering factors of Ge and Al would induce relatively intense diffuse scattering on the above-mentioned position. No such scattering is observed in these samples.

Weak additional features appear in diffraction patterns for compositions with $x > 0.20$ in germanium mullites. The diffuse scattering intensity increases with x and at the same time these features seem to sharpen. A blurred halo is first observed around the $1,0,\frac{1}{2}$ mullite position and with increasing x values two satellites are resolved around this position. Cameron (*6*) and then Ylä-Jääski and Nissen (*19*) related the spacing between these two satellites to the composition for silicon mullites. However, the diffuse scattering pattern also depends on the annealing temperature. For example, Fig. 4 shows two different diffraction patterns that we obtained on germanium mullites with the same composition ($x = 0.40$) but which were annealed at different temperatures.

For the same composition, the scattered intensity is not weaker in silicon mullites than in the corresponding germanates. As Ge/Al ordering would result in much higher scattered intensity than Si/Al ordering, this indicates that the diffuse scattering results

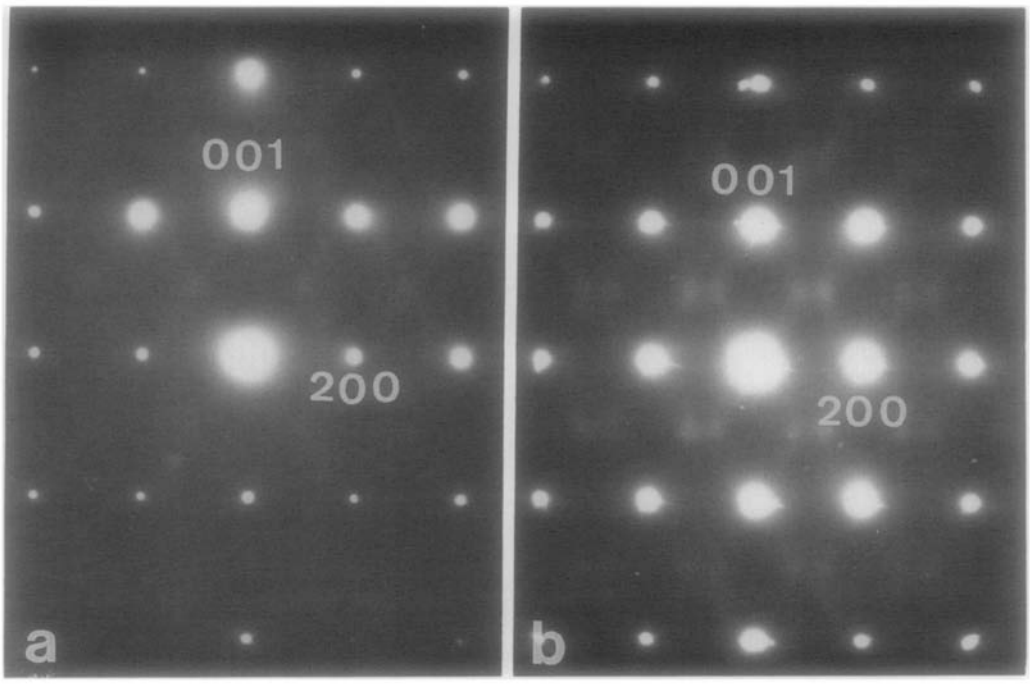

FIG. 4. Electron diffraction patterns of (010) planes of a 2 : 1 mullite $Al_{4+2x}Ge_{2-2x}O_{10-x}$ ($x = 0.40$) (a) as prepared at 1550°C, (b) after annealing 24 hr at 1300°C.

from oxygen vacancy rather than from cation ordering. Figure 5 shows two very similar diffraction patterns for Si and Ge phases with the 2 : 1 composition ($x = 0.4$).

HRTEM Observations and Digital Image Processing

Previous HRTEM observations of the (010) plane, in particular the work of Ylä-Jääski and Nissen (*19*), revealed superstructures in silicon mullites with a high rate of oxygen vacancies. These are commonly described in terms of antiphase domain structures owing to the similarity of the images obtained with those of metallic alloys for example. In fact what is referred to an antiphase boundary is nothing more than the contrast due to the ordering scheme of oxygen vacancies. According to the models proposed by Ylä-Jääski and Nissen (*19*) from HRTEM observations and their interpretations after image simulations, vacancies are aligned to form channels parallel to the *b* direction. In projection on the (010) plane, these channels form zigzag chains. For particular compositions, these chains are found to be parallel to [001]. In this case, they exactly correspond to the "mullite" chains introduced by Saalfeld (*34*) from a Patterson analysis of the satellite reflections of mullite. For compositions with x close to 0.4, our HRTEM images of Ge mullites do not reveal a perfectly ordered superstructure when observed over a large area (Fig. 6). However, locally we find regions with higher degrees of order, as shown in Fig. 7. This image is quite comparable to that obtained on an ordered Si mullite by Ylä-Jääski and Nissen [Fig. 5 of Ref. (*19*)]. It seemed thus likely that the ordering scheme proposed for high vacancy Si mullites (*19*) could also apply to homologous germanates. In order to verify

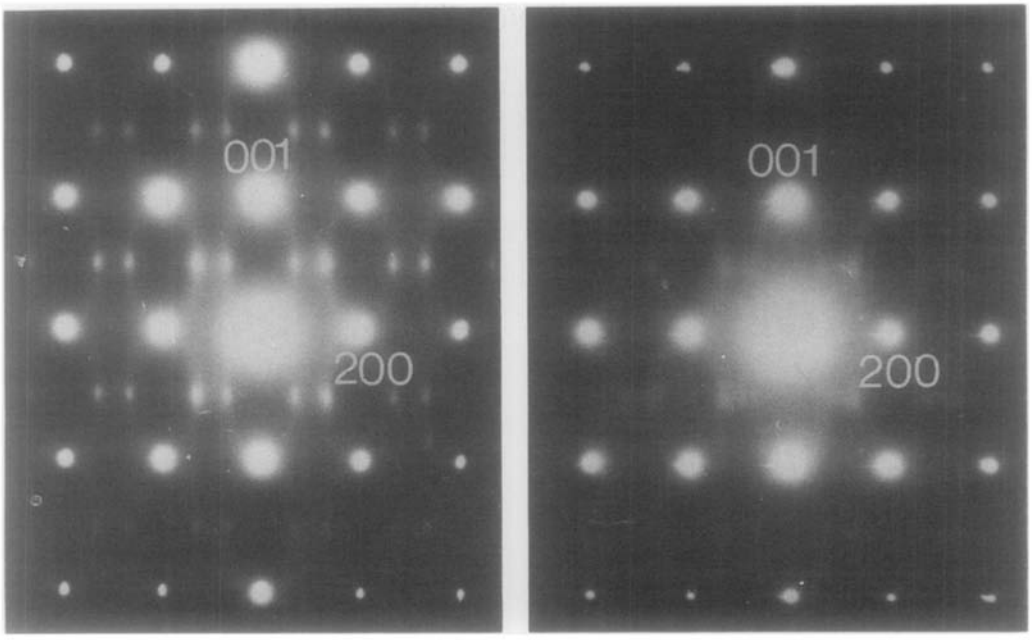

FIG. 5. Electron diffraction patterns of (010) planes of 2 : 1 mullites $Al_{4+2x}M_{2-2x}O_{10-x}$ ($x = 0.40$) (a) silicon mullite crystal grown from the melt (b) germanium phase (prepared at 1550°C and annealed 24 hr at 1300°C).

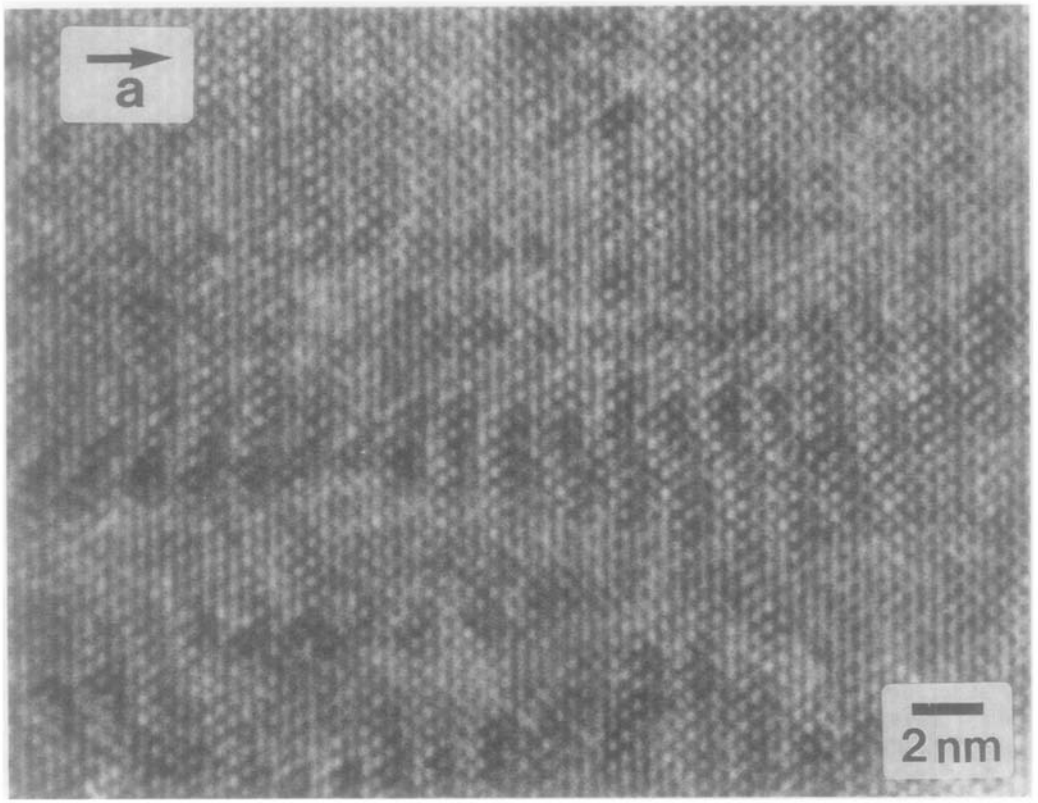

FIG. 6. HRTEM image of a germanium mullite with composition close to 2 : 1 ($x \approx 0.4$) prepared at 1550°C and annealed 24 hr at 1300°C. Electron beam parallel to [010] direction.

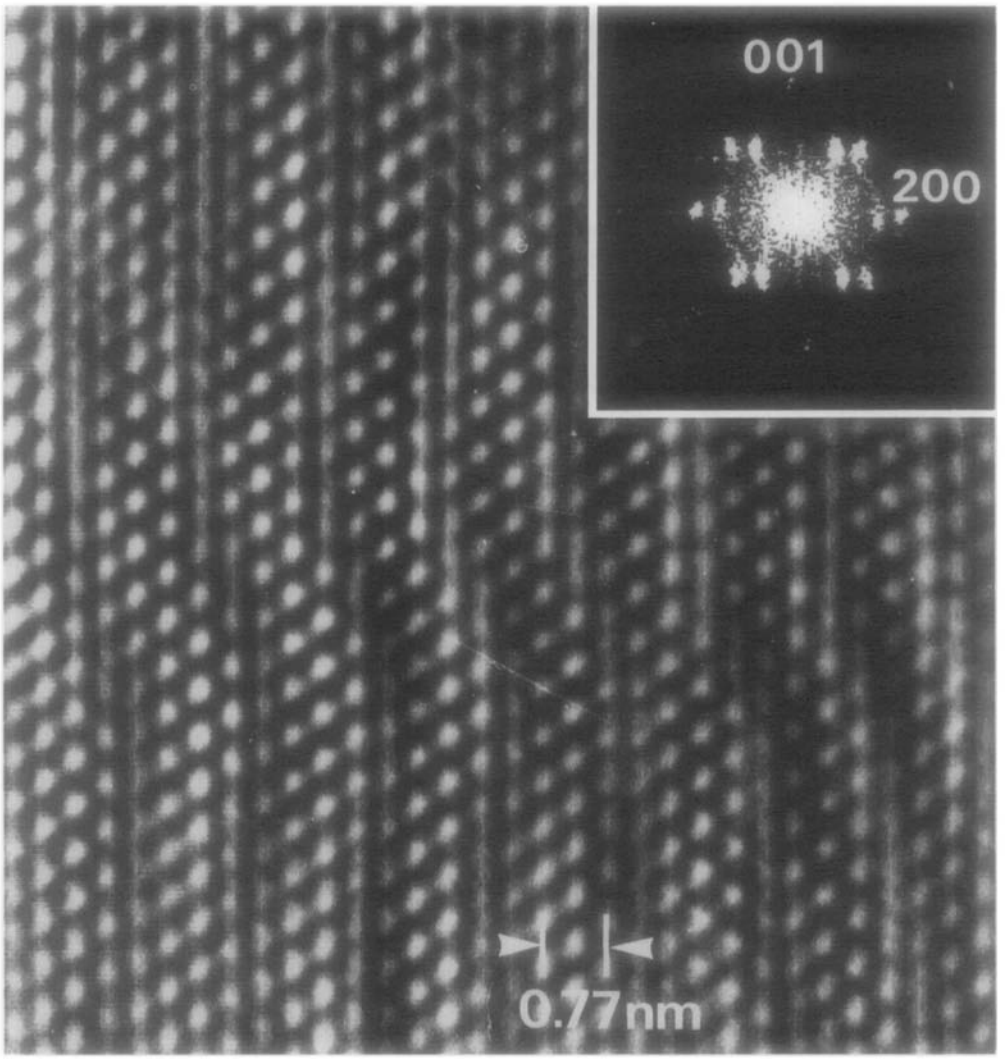

FIG. 7. Digitized image of an ordered region observed on the same sample with the same orientation as in Fig. 6. Inset shows the diffraction obtained from this image.

this hypothesis, we have simulated the contrast of a Ge mullite superstructure using the model of vacancy ordering along *b*, which is schematically represented on Fig. 8. Atomic positions are derived after locating oxygen vacancies on zigzag chains, using data of the average structure from Ref. (*26*). The structure given in Table I for a composition $x = 0.5$ corresponds to quadrupling of *a* and doubling of *c* mullite parameters and contains four formula groups $Al_{10}Si_2O_{19}$ per unit cell. Its space group is $Cmc2_1$ in a standard setting, but atomic positions are referred to $Bb2_1m$ in order to allow a comparison with mullite without permutation of axis. Nevertheless, a translation of origin is needed to derive the superstructure from mullite, the origin of this latter, being on

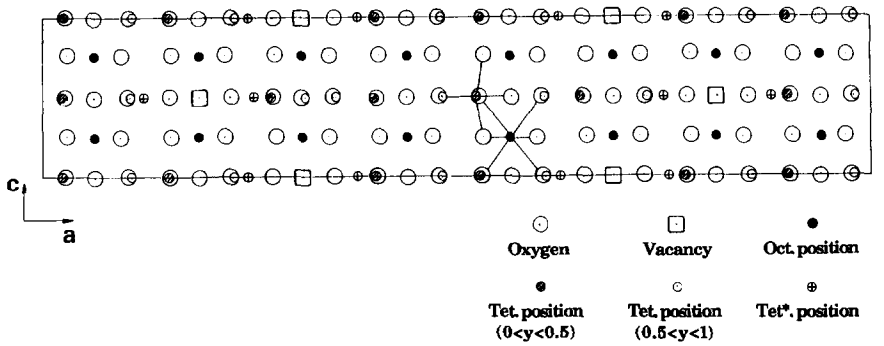

FIG. 8. (010) projection of the superstructure model for $Al_{10}Si_2O_{19}$ ($x = 0.5$).

TABLE I

ATOMIC POSITIONS OF A MULLITE SUPERSTRUCTURE $Al_{10}M_2O_{19}$ (M = Si or Ge) USING AVERAGE POSITIONS DERIVED FROM (*26*)

Space group $Bb2_1m$ (No. 36), $Z = 4$ (origin on $b2_1m$)
Unit cell constants $a = 4a_{mullite}$, $b = b_{mullite}$, $c = 2c_{mullite}$

	Wyckoff position	x	y	z
Oct 1	8b	0.062	0.000	0.250
Oct 2	8b	0.312	0.000	0.250
Tet 1	4a	0.100	0.340	0
Tet 2	4a	0.600	0.340	0
Tet 3	4a	0.850	0.340	0
Tet 4	4a	0.775	0.660	0
Tet 5	4a	0.525	0.660	0
Tet 6	4a	0.025	0.660	0
Tet* 1	4a	0.380	0.205	0
Tet* 2	4a	0.247	0.795	0
O1	4a	0.152	0.422	0
O2	4a	0.652	0.422	0
O3	4a	0.402	0.422	0
O4	4a	0.902	0.422	0
O5	4a	0.223	0.578	0
O6	4a	0.723	0.578	0
O7	4a	0.472	0.578	0
O8	4a	0.972	0.578	0
O9	8b	0.094	0.219	0.250
O10	8b	0.344	0.219	0.250
O11	8b	0.281	0.781	0.250
O12	8b	0.531	0.781	0.250
O_c1	4a	0.425	0.050	0
O_c2	4a	0.200	0.945	0
O_c3	4a	0.937	0.000	0
Oxygen vacancy	4a	0.687	0.00	0

an inversion center for the *Pbam* group, is translated to $b2_1m$ for the noncentrosymmetric $Bb2_1m$ group. Using this model, a computed image with contrast similar to that of the experimental image (Fig. 7) can be obtained for an underfocus in the range of 20–40 nm and a thickness of 12–18 nm. Various cation distributions were tried: (a) disorder of Al and Ge on all sites (tetrahedral and octahedral), (b) Al on octahedra and disorder on tetrahedral sites only, (c) full ordering assuming that Al are on octahedral sites and on all the tetrahedral sites surrounding the O_c atoms common to the three tetrahedra. With our microscope and for the conditions of thickness and defocus mentioned above, the difference in image contrast between the three cationic distributions tried is so insignificant that no information can be drawn on cation locations. Moreover, a very similar image is obtained, replacing Ge by Si in the calculations. Results of these simulations are given in Fig. 9, the brighter spots correspond to the location of [010] rows of oxygen vacancies. These simulated images are quite similar to those obtained by Ylä-Jääski and Nissen on a silicon mullite (*19*).

A (001) projection of the superstructure is given in Fig. 10. Only tetrahedral arrays are represented for clarity of observation, as octahedral positions remain unaffected by the ordering scheme. Making reference to

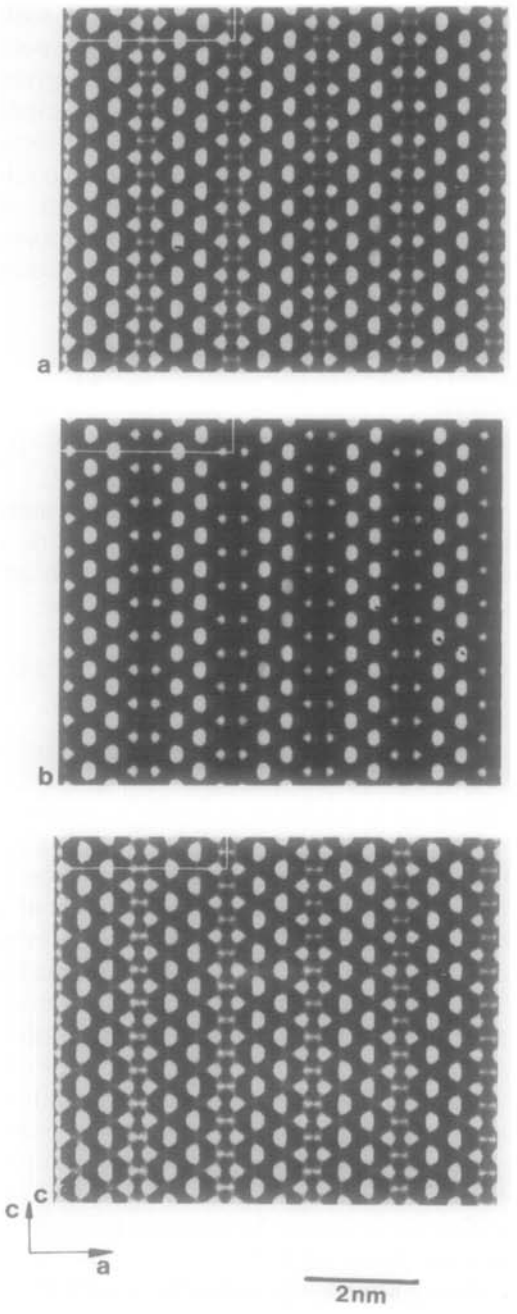

FIG. 9. Simulated images on a (010) plane using the structure given in Table I, with the various cationic distributions (a) total disorder of Al and Ge on all cationic sites, (b) full ordering assuming Al on octahedra and on tetrahedra surrounding O_{1c} atoms, (c) replacing Ge by Si in the calculations; due to the close scattering factor of Al and Si the image contrast is unaffected by the cationic distribution. The following parameters were selected: beam divergence = 1 mrad, chromatic defocus = 7.5 nm, aperture = 4 $(nm)^{-1}$, number of beams used for the dynamical calculations = 331, sample thickness = 18 nm, and underfocus = 35 nm. The origin of the unit cell is at the top left corner of the image and brighter spots correspond to the projection of rows of oxygen vacancies.

the nomenclature of Saalfeld, we can observe both sillimanite (S) and mullite (M) double chains with oxygen vacancies located within the latter. Looking perpendicular to the *a* axis, slices containing M and S chains are alternately found.

This model corresponds to a rate of oxygen vacancy ($x = 0.5$, i.e., 83.3 atom% Al) which is higher than the nominal composition of our samples. TEM energy dispersive analysis gives an average composition of 81 ± 1 atom% of Al for the observed zones. However, we are not certain that the local composition of regions with highly ordered structure are equivalent to the average value. It is also possible that the defects present in the real structure account for the discrepancy of its composition from that of the model.

In contrast with highly ordered structures previously described, we have observed, in samples with lower concentrations of alumina, structures with short-range order only. The diffuse scattering features are not as well defined in such cases. In a previous paper (*38*), we reported HRTEM observations in which the intensity of white dots located at the nodes of the mullite lattice projected along [010] was fluctuating. In particular, HRTEM images are different, depending on the position of the objective aperture. Examples are given in Fig. 11 for a 2:1 silicon mullite ($x = 0.4$). With a diaphragm centered on the diffuse scattering and including Bragg spots (Fig. 11a), the basic lattice of mullite is observed, whereas a modulated contrast is revealed when the diffuse features only are selected (Fig. 11b).

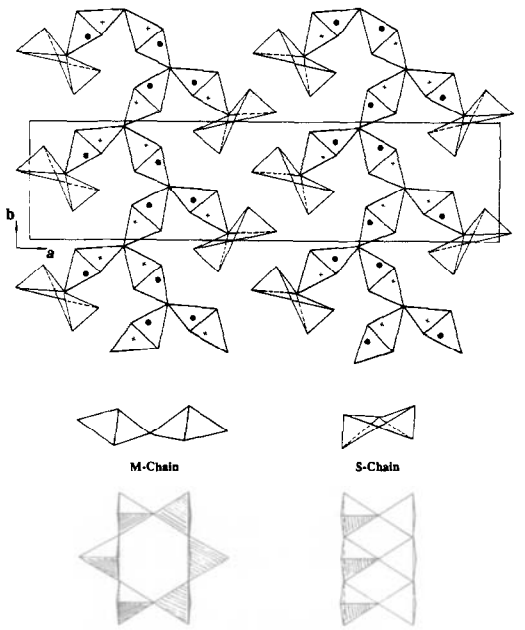

FIG. 10. (001) projection of the superstructure model for $Al_{10}Si_2O_{19}$ ($x = 0.5$). Only tetrahedra are represented, they form the M and S double-chains. Centers of M-chain tetrahedra at $c = 0$ (×) and $\frac{1}{2}$ (●). M- and S-chains are represented on the lower part of the figure parallel to c.

This can be attributed to short range order. Similarly, Ylä-Jääski and Nissen (*19*) reported that in silicon mullites, for $x = 0.4$, they observed clusters of white dots on HRTEM images, but that no long range correlation between the clusters existed.

Digital image processing has been used to draw out the information relative to short range order from HRTEM images. Most of the original images consist of an array of dots with variable intensity located on the nodes of a periodic lattice. The diffraction pattern of such an object is similar to that of a mixed crystal—e.g., a disordered alloy—in which the structure factor F_m for a unit-cell defined by a vector $\mathbf{x}_m$ is not constant from one cell m to another n. The diffraction theory of such imperfect lattices has been extensively treated by Guinier (*44*). The diffraction pattern consists of Bragg peaks on reciprocal lattice positions with additional diffuse scattering. Bragg spots correspond to the diffraction of a perfect lattice where all unit-cells have a structure factor equal to the mean factor $\bar{F}$. The location of diffuse scattering depends on the relative positions of the various dots (for an image) or atoms (for a crystal). The intensity $I_{(\mathbf{q})}$ of the diffuse scattering for a reciprocal vector $\mathbf{q}$ is given by a Fourier series:

$$I_{(\mathbf{q})} = \Sigma \Phi_m \exp(2\pi i \mathbf{q} \cdot \mathbf{x}_m),$$

where

$$\Phi_m = |\overline{F_n F^*_{n+m}}| - |\bar{F}|^2 \qquad (1)$$

This intensity is periodic if the coefficients Φ_m are independent of $\mathbf{q}$. In this case, they can be obtained by Fourier inversion according to:

$$\Phi_m = v \int I_{(\mathbf{q})} (\exp(-2\pi i \mathbf{q} \cdot \mathbf{x}_m)\, dv_{\mathbf{q}}, \qquad (2)$$

where v is the cell volume.

In fact, $I_{(\mathbf{q})}$ is not periodic because atomic scattering factors decrease with $\mathbf{q}$. Nevertheless, Eq. (2) leads generally to approximate values of Φ_m by Fourier transform of the diffuse scattering pattern. According to these remarks, the average structure of a mixed crystal can be reconstructed by Fourier transform of the fundamental peaks. This defines a periodic lattice with an average intensity $\bar{F}$ for all $\mathbf{x}_m$. In addition, information on ordered arrangements can be obtained by Fourier inversion of the diffuse scattering. The resulting intensity in direct space for a given $\mathbf{x}$ will be approximately the coefficient Φ_m, which is related to the difference between the structure factor in $\mathbf{x}_m$ and the mean value $\bar{F}$.

Image processing allows the experimental selection of either the Bragg spots or the diffuse scattering in the Fourier transform of a digitized HRTEM image. This can be done by multiplying the value of the Fourier transform for each pixel by a unit value in the areas of interest (Bragg spots or diffuse

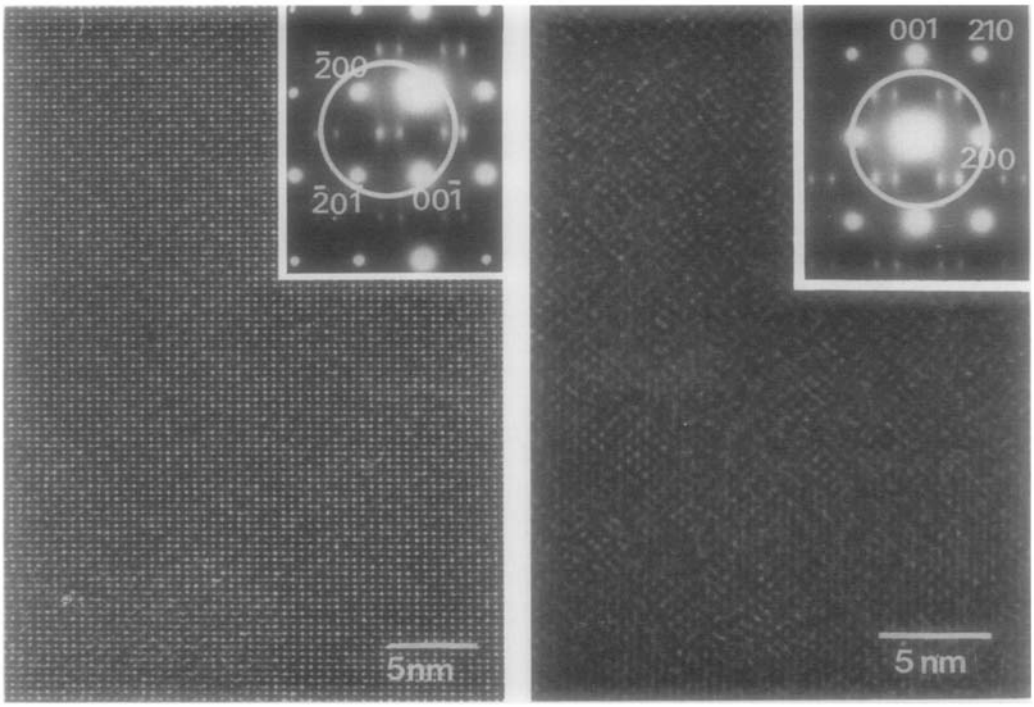

FIG. 11. HRTEM images of 2 : 1 silicon mullite ($x = 0.4$) as grown from the melt. Plane of observation (010). The apertures used for obtaining the images are given in insets on the experimental diffraction patterns: (a) image formed with diffuse scattering and Bragg spots (left), (b) image formed with the central spot and diffuse features only (right).

scattering) and by a null value outside. Practically, we used circular marks with appropriate radii centered on Bragg spots and diffuse features.

The diffraction pattern of an original image obtained on a 2 : 1 Si mullite shows diffuse scattering around the 1, 0, $\frac{1}{2}$ position (Fig. 12a). The image has been reconstructed from inverse Fourier transform after selecting both Bragg positions and diffuse scattering (Fig. 12b), only Bragg positions (Fig. 12c), or only the diffuse scattering (Fig. 12d). The masks used are shown in the insets. The image in Fig. 12b is nearly the same as the original but its quality is improved due to the filtering of low frequency noise. As expected, the image in Fig. 12c corresponds to the projected lattice of the average mullite structure. More interesting is Fig. 12d on which the location of bright dots perceivable in Fig. 12b can be better visualized. Brighter dots are clustered in domains of a few nanometers. Inside these domains, the periodicity along [001] is twice that of the average structure of mullite (5.8 nm). In addition, the contrast inside these domains is similar to that observed for long range ordered superstructures in germanium mullites (Fig. 7) or silicon mullites (*19*).

Similar features have been also well observed on various samples of silicon or germanium phases for compositions ranging between 3 : 2 and 2 : 1 mullite ($0.25 < x < 0.4$). Figure 13 shows an image relative to a 3 : 2 germanium mullite ($x = 0.25$) annealed at 1300°C. The domain structure revealed by inverse Fourier transform of the diffuse

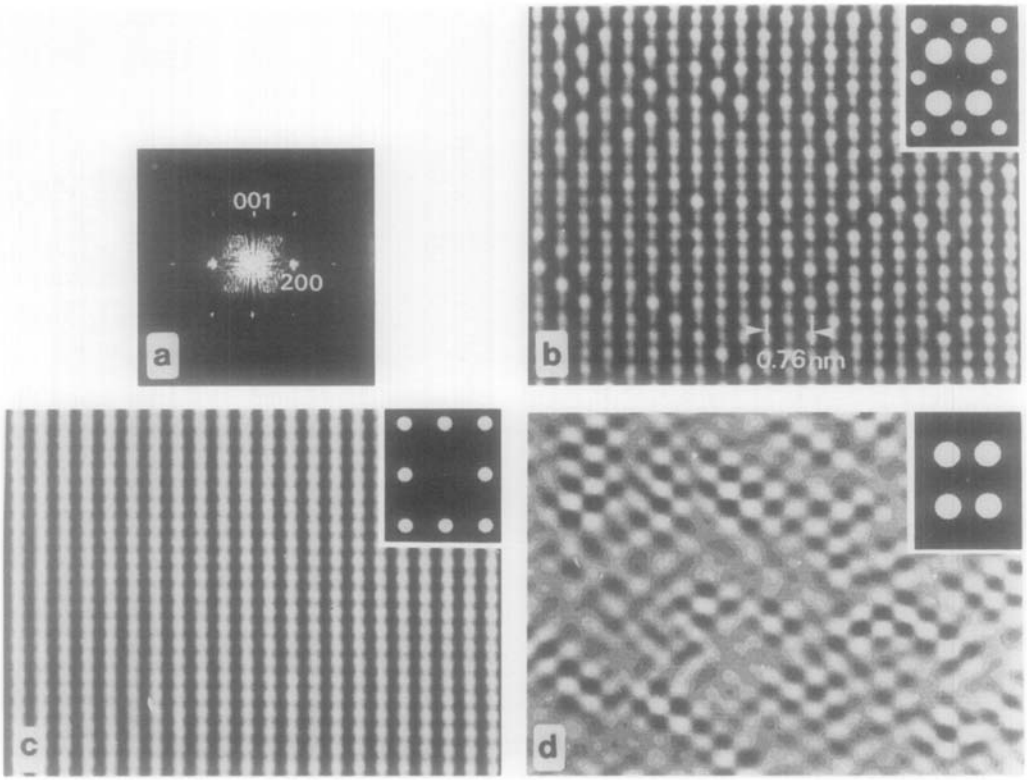

FIG. 12. Fourier filtering of a digitized image corresponding to the same sample and orientation as Fig. 11: (a) diffraction pattern of the image in logarithmic scale, (b) image reconstructed using both Bragg spots and diffuse scattering, (c) average mullite structure obtained with Bragg spots only, (d) domain structure revealed from Fourier inversion of diffuse scattering. In the last three images the reciprocal space is represented in the inset at the same scale as the diffraction pattern in a. Only areas located within the circular masks are used for image reconstruction.

scattering is quite comparable to the features observed on a Si analog.

These results demonstrate a trend for the formation of ordered zones within a disordered mullite matrix. Inside these domains we observe HRTEM image contrast showing similarities with those of superstructures observed by Ylä-Jääski and Nissen (*19*) and us. In particular a doubling of the *c* periodicity is observed systematically. It is therefore likely that these domains correspond to a region of high vacancy concentration with local arrangements similar to those found in these superstructures. At present it is not possible to give a more precise description of short-range ordering in these domains. Work is in progress to attempt to correlate the evolution of order as a function of composition and annealing. A major difficulty arises from the possible existence of areas with variable degrees of order and local composition even though the average composition of samples is carefully analyzed. A combination in the same microscope of local analysis with a nanoprobe, HR observation, and diffraction at the same scale would be helpful to assure a precise measurement of the composition of the zones examined.

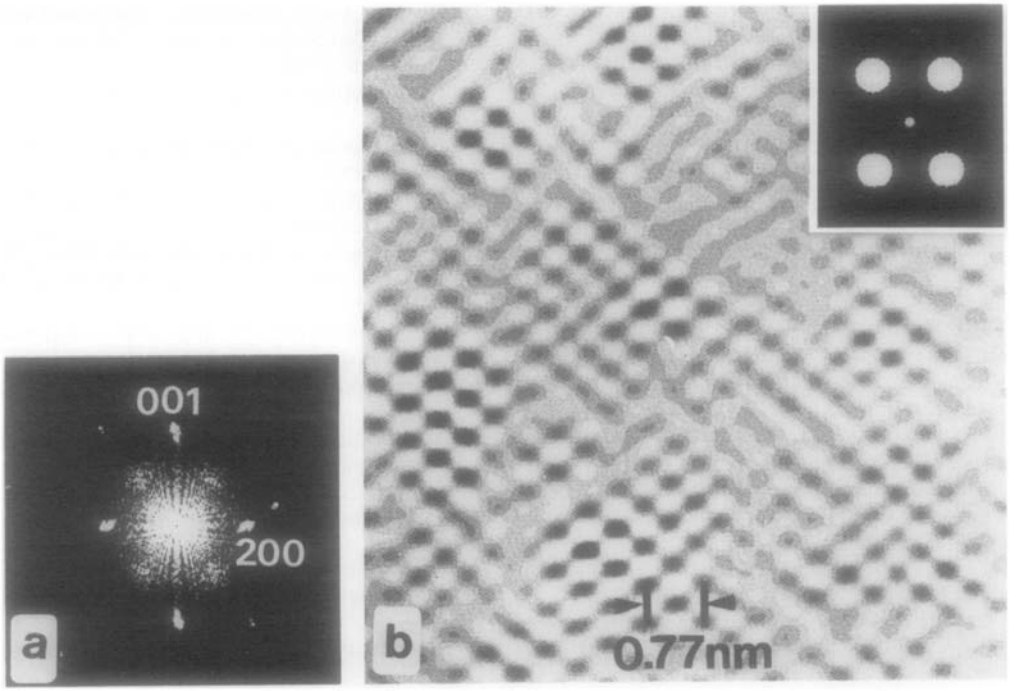

FIG. 13. Fourier filtering of a HRTEM (010) image of a 3 : 2 germanium mullite ($x = 0.25$): (a) diffraction pattern of the image in logarithmic scale, (b) domain structure revealed from Fourier inversion of diffuse scattering around 1, 0, $\frac{1}{2}$ and equivalent positions (centers of the circular marks given in the inset).

Conclusion

This study has demonstrated the complexity of ordering phenomena in mullites, which depend on both the composition and the thermal history of samples, and has confirmed that oxygen vacancies are primarily responsible for the observed diffuse scattering. For a high rate of oxygen vacancy ($x > 0.4$), HRTEM images on germanium, mullites show the formation of a superstructure, the structure of which was derived from image simulations. The model is identical to one of those proposed by Ylä-Jääski and Nissen (*19*).

For lower rates of oxygen vacancy, short range order domains have been revealed from HRTEM observations after digital processing of diffuse scattering. The precise arrangement inside domains has to be completed by further work; however, the contrast and periodicity of these domains suggest a close relationship with structures having long range order.

Acknowledgments

The authors are indebted to Dr. P. Bariand (Laboratory of Mineralogy, University of Paris) for providing us with crystals of natural sillimanite.

References

1. N. L. BOWEN AND J. V. GREIG, *J. Amer. Ceram. Soc.* **7**, 238 (1924).
2. S. ARAMAKI AND R. ROY, *J. Amer. Ceram. Soc.* **45**, 229 (1962).
3. I. A. AKSAY AND J. A. PASK, *J. Amer. Ceram. Soc.* **58**, 507 (1975).
4. F. J. KLUG, S. PROCHAZKA, AND R. H. DOREMUS, *J. Amer. Ceram. Soc.* **70**, 750 (1987).

5. W. E. CAMERON, *Amer. Ceram. Soc. Bull.* **56,** 1003 (1977).
6. W. E. CAMERON, *Amer. Mineral.* **62,** 747 (1977).
7. M. PEREZ Y JORBA, *Rev. Int. Hautes Temp. Réfract.* **6,** 283 (1969).
8. D. MICHEL, S. ABOLHASSANI, A. KAHN, V. AGAFONOV, AND M. PEREZ Y JORBA, *in* "Ceramic Transactions," (S. Somiya, R. F. Davis, J. A. Pask, Eds.), Vol. 6, p. 159. The American Ceramic Society, Westerville (1990).
9. S. P. CLARK, E. C. ROBERTSON, AND F. BIRCH, *Amer. J. Sci.* **255,** 628 (1957).
10. M. J. HOLDAWAY, *Amer. J. Sci.* **271,** 97 (1971).
11. W. H. TAYLOR, *Z. Kristallogr.*, **68,** 503-21 (1928).
12. H. SCHOLZE, *Ber. Dtsch. Keram. Ges.* **32,** 381 (1955).
13. S.O. AGRELL AND J. V. SMITH, *J. Amer. Ceram. Soc.* **43,** 69 (1960).
14. S. DUROVIC, *J. Amer. Ceram. Soc.* **45,** 157 (1962).
15. R. SADANAGA, M. TOKONAMI, AND Y. TAKEUCHI, *Acta Crystallogr.* **15,** 65 (1962).
16. C. W. BURNHAM, *Carnegie Inst. Washington Yearbook* **6,** 227 (1964).
17. C. W. BURNHAM, *Z. Kristallogr.* **118,** 128 (1963).
18. L. W. FINGER AND E. PRINCE, *Carnegie Inst. Washington Yearbook* **71,** 496 (1972).
19. J. YLÄ-JÄÄSKI AND H. U. NISSEN, *Phys. Chem. Minerals* **10,** 47 (1983).
20. P. A. FORSTER, *J. Electrochem. Soc.* **106,** 971 (1959).
21. P. H. DUVIGNEAUD, *J. Amer. Ceram. Soc.* **57,** 224 (1974).
22. A. J. PERROTTA AND J. E. YOUNG, JR., *J. Amer. Ceram. Soc.* **57,** 405 (1974).
23. C. W. BURNHAM, *Carnegie Inst. Washington Yearbook* **62,** 158 (1962) and **63,** 223 (1963).
24. S. DUROVIC, *Slovak Acad. of Sci. Chem Zvesti* **23,** 113 (1969).
25. H. SAALFELD AND W. GUSE, *N. Jahrb. Min. Mh.*, 145 (1981).
26. R. J. ANGEL AND C. T. PREWITT, *Amer. Mineral.* **71,** 1476 (1986).
27. S. DUROVIC, P. FEJDI, *Silicaty* **2,** 97–112 (1976).
28. W. GUSE AND H. SAALFELD, "Mullite and Mullite Matrix Composites," Ceramic Transactions, (S. Somiya, R. F. Davis, J. A. Pask, Eds.), Vol. 6, p. 73, The American Ceramic Society, Westerville (1990).
29. Y. NAKAJIMA AND P. H. RIBBE, *Amer. Mineral.* **66,** 142 (1981).
30. W. M. KRIVEN AND J. A. PASK, *J. Amer. Ceram. Soc.* **66,** 649–654 (1983).
31. H. R. WENK, *N. Jahrb. Min. Abh.* **146,** 1 (1983).
32. W. GUSE AND H. SAALFELD, *Z. Kristallogr.* **143,** 177 (1976).
33. M. TOKONAMI, Y. NAKAJIMA AND N. MORIMOTO, *Acta Crystallogr.* **A36,** 270 (1980).
34. H. SAALFELD, *N. Jahrb. Min. Abh.* **134,** 305 (1979).
35. Y. NAKAJIMA, N. MORIMOTO, AND E. WATANABE, *Proc. Japan Acad.* **51,** 173 (1975).
36. D. SCHRYVERS, K. SRI KRISHNA, M. A. O'KEEFE, AND G. THOMAS, *J. Mater. Res.* **3,** 1355 (1988).
37. J. D. C. MCCONNELL AND V. HEINE, *Phys. Rev. B* **31,** 6140 (1985).
38. D. MICHEL, L. MAZEROLLES, AND R. PORTIER, "Ceramic Transactions," (S. Somiya, R. F. Davis, J. A. Pask, Eds.), Vol. 6, p. 435, The American Ceramic Society, Westerville (1990).
39. W. GUSE AND D. MATEIKA, *J. Cryst. Growth* **22,** 237 (1974).
40. V. AGAFONOV, A. KAHN, D. MICHEL, M. PEREZ Y JORBA, AND M. FEDOROFF, *J. Cryst. Growth* **71,** 256 (1985).
41. V. AGAFONOV, A. KAHN, D. MICHEL, M. PEREZ Y JORBA, AND M. FEDOROFF, *J. Solid State Chem.* **62,** 402 (1986).
42. M. CORNIER-QUIQUENDON, "Dynamical theory of the diffraction of fast electrons by crystals and quasicrystals," Thesis University Paris VI (1988).
43. M. PEREZ Y JORBA, P. TARTE, AND R. COLLONGUES, *C.R. Acad. Sci. Paris* **257,** 3417 (1963).
44. A. GUINIER, "Theorie et Technique de la radiocristallographie," Chapter XIII, p. 490–636, Dunod, Paris (1964).